Proceedings of the 3rd ITB Graduate School Conference ISSN: 2963-718X
Enhancing Creativity in Research Through Developing Innovative Capabilities
December 21, 2022

Deformation Monitoring of Lava Dome Growth derived by Sentinel-1A images at Mt. Ibu, North Maluku, Indonesia

Nur Ayu Anas & Asep Saepuloh*

Geological Engineering, Faculty of Earth Sciences and Technology, Bandung Institute of Technology, Jl. Ganesha No. 10, bandung, Indonesia.
*Email: saepuloh@itb.ac.id

Abstract. Understanding the growth of lava domes in volcanoes is one of the most important tasks in volcanology because of the high threat to human life and infrastructure. One of the volcanoes with high lava dome growth is Mt. Ibu in North Maluku Province, Indonesia. Monitoring the growth of the lava dome on Mt. Ibu relied on the visual camera at the observation post. Therefore, the growth of the dome could only be observed from a few vantage points. To resolve this problem, the Sentinel-1A images have been used to monitor the area and volume lava dome regardless of cloud cover or ash plume from the eruption of Mt. Ibu. The current condition of the lava dome has expanded through the outer crater rim in the northern flank, which is about 5 km from urban areas. We used the pair-wise logic technique differential interferometric synthetic aperture radar (PLT D-InSAR) method to monitor the deformation of the lava dome growth from January 2020 to September 2022. The PLT D-InSAR deformation results show that the highest uplift and subsidence occurred in January 2022 about 0.667 m and in August 2020 about -0.48 m, respectively. The k-means clustering, median, and open filtering methods were also used to enhance the contrast of the deformation areas.

Keywords: *Deformation; PLT D-InSAR; K-Means clustering.*

1 Introduction

The existence of a lava dome on a volcano can cause a significant hazard when it becomes unstable and collapse [1]. Apart from instability, other things that can cause the collapse of a lava dome are related to the morphology and internal structure of the lava dome [2]. Examples of lava dome hazards have been occurred on Mt. Merapi and St. Helens. The 2010 Mt. Merapi eruptions occurred due to destructive pyroclastic density currents (PDCs) from the collapse of a lava dome with an area of more than15 km from the summit and caused the evacuation of one-third of one million people around Mt. Merapi [3]. Then on Mt. St. Helens, there was also lava dome eruptions that began with an explosive episode in 1980, which produced eruptive columns 13-15 km above sea level and pyroclastic flows down the northern flank of the volcano [4]. Examples of events on Mt. Merapi and St. Helens are the phenomenon to worry. One of Indonesia's volcanoes with a lava dome is Mt. Ibu, located in North Maluku Province, Indonesia (Figure 1).

Mt. Ibu is a stratovolcano where the growth of the lava dome needs to be monitored and worried because the lava dome has reached the outer crater rim on the north side. The differential interferometric synthetic aperture radar (D-InSAR) method is one way to monitor deformation. The method has been applied to observe the changes in the soil surface prior to the major eruption of Mt. Merapi in 2010 and to detect pre- and syn-eruptive signatures on Mt. Sinabung [5], [6]. Then the method developed into the pair-wise logic technique (PLT) D-InSAR, which has simple arithmetic to reduce the effect of the atmosphere on the image [7]. Based on this, the PLT D-InSAR method has been used to monitor the deformation of the Mt. Ibu. Deformation can be monitored by this method either in the form of subsidence or uplift. Then, the deformations obtained have been clustered using k-means and filtered using median open filtering. Accordingly, deformation monitoring at Mt. Ibu is necessary because the growth of the lava dome can be observed beyond the surface. We have used Sentinel-1A images to obtain deformation at the summit lava dome regardless of cloud cover or ash from the eruptions.

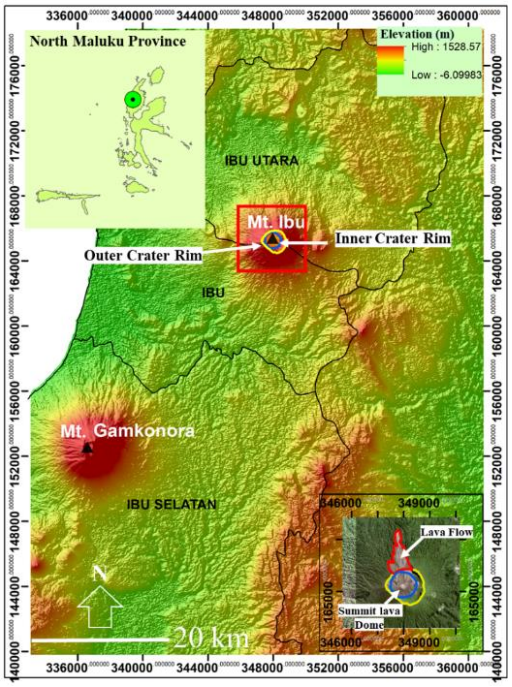

Figure 1 Location of Mt. Ibu given a red rectangle; at the top of Mt. Ibu has an inner crater rim (blue line) and an outer crater rim (yellow line). Then the below inset shows the summit of a lava dome and lava flow (red line).

2 Data used

This study used Sentinel-1A imagery with IW (interferometric wide-swath) beam mode acquisition, single look complex (SLC) file type, and C-band. We have used VV polarization because it can show up and down patterns on deformation correctly, as suggested by previous published study [8]. We have used three bursts from sub-swaths from 1 to 3 from January 2020 to August 2022 (**Table 1**). An example of Sentinel-1A images is shown in **Figure 2**.

Table 1. Sentinel 1A acquisition data.

Number	ID Scene	Acquisition	Polarization	Orbit	Abs Orbit
1	S1A_IW_SLC__1SDV_ 20200113 T21173620200113 T211803030787_0387F5_1019	13 January 2020	VV+VH	Descending	30787
2	S1A_IW_SLC__1SDV_202002 18T21173520200218T211802 031312_039A46_6113	18 February 2020	VV+VH	Descending	31312
3	S1A_IW_SLC__1SDV_202003 25T21173520200325T211802 _031837_03AC8B_4702	25 March 2020	VV+VH	Descending	31837
4	S1A_IW_SLC__1SDV_202004 18T211736_20200418T211803 _032187_03B8DA_D313	18 April 2020	VV+VH	Descending	32187
5	S1A_IW_SLC__1SDV_202005 24T21173820200524T211805 _032712_03CA0A_A7E6	24 May 2020	VV+VH	Descending	32712
6	S1A_IW_SLC__1SDV_202006 17T211739_20200617T211806 _033062_03D47A_D2CE	17 June 2020	VV+VH	Descending	33062
7	S1A_IW_SLC__1SDV_202007 11T211741_20200711T211808 _033412_03DF1B_82E1	11 July 2020	VV+VH	Descending	33412
8	S1A_IW_SLC__1SDV_202008 16T21174320200816T211810 _033937_03EFEA_1BA1	16 August 2020	VV+VH	Descending	33937
9	S1A_IW_SLC__1SDV_202009 21T211744_20200921T211811 _034462_04027B_CCA4	21 September 2020	VV+VH	Descending	34462
10	S1A_IW_SLC__1SDV_202010 15T211745_20201015T211812 _034812_040EB2_2D46	15 October 2020	VV+VH	Descending	34812
11	S1A_IW_SLC__1SDV_202011 20T211744_20201120T211811 _035337_0420DC_DE53	20 November 2020	VV+VH	Descending	35337
12	S1A_IW_SLC__1SDV_202012 26T211743_20201226T211810	26 December 2020	VV+VH	Descending	35862

	_035862_0432FF_FCEF				
13	S1A_IW_SLC__1SDV_20210119T211742_20210119T211809_036212_043F38_E99B	19 January 2021	VV+VH	Descending	36212
14	S1A_IW_SLC__1SDV_20210212T21174120210212T211808_036562_044B5A_5887	12 February 2021	VV+VH	Descending	36562
15	S1A_IW_SLC__1SDV_20210320T21174120210320T211808_037087_045DAB_F6D3	20 March 2021	VV+VH	Descending	37087
16	S1A_IW_SLC__1SDV_20210425T21174220210425T211809_037612_046FCA_12FA	25 April 2021	VV+VH	Descending	37612
17	S1A_IW_SLC__1SDV_20210519T21174320210519T211810_037962_047B09_05CC	19 May 2021	VV+VH	Descending	37962
18	S1A_IW_SLC__1SDV_20210624T21174620210624T211812_038487_048AB1_1D49	24 June 2021	VV+VH	Descending	38487
19	S1A_IW_SLC__1SDV_20210718T21174720210718T211814_038837_049537_E317	18 July 2021	VV+VH	Descending	38837
20	S1A_IW_SLC__1SDV_20210811T21174820210811T211815_039187_04A025_7E23	11 August 2021	VV+VH	Descending	39187
21	S1A_IW_SLC__1SDV_20210928T21175020210928T211817_039887_04B830_6CED	28 September 2021	VV+VH	Descending	39887
22	S1A_IW_SLC__1SDV_20211022T21175120211022T211818_040237_04C451_9F29	22 October 2021	VV+VH	Descending	40237
23	S1A_IW_SLC__1SDV_20211127T211750 20211127T211817_040762_04D686_C915	27 November 2021	VV+VH	Descending	40762
24	S1A_IW_SLC__1SDV_20211221T21174920211221T211816_041112_04E274_D059	21 December 2021	VV+VH	Descending	41112
25	S1A_IW_SLC__1SDV_20220126T211747 20220126T211814_041637_04F410_76A5	26 January 2021	VV+VH	Descending	41637
26	S1A_IW_SLC__1SDV_20220207T21174720220207T211814_041812_04FA14_0DFC	7 February 2022	VV+VH	Descending	41812
27	S1A_IW_SLC__1SDV_20220327T21174720220327T211814_042512_051208_5225	27 March 2022	VV+VH	Descending	42512

28	S1A_IW_SLC__1SDV_20220420T211748202204 20T211815_042862_051DCB_37D4	20 April 2022	VV+VH	Descending	42862
29	S1A_IW_SLC__1SDV_20220526T211750202205 26T211816_043387_052E61_2B31	26 May 2022	VV+VH	Descending	43387
30	S1A_IW_SLC__1SDV_20220619T211751202206 19T211818_043737_0538C5_5881	19 June 2022	VV+VH	Descending	43737
31	S1A_IW_SLC__1SDV_20220701T211752202207 01T211819_043912_053E00_BBBD	1 July 2022	VV+VH	Descending	43912
32	S1A_IW_SLC__1SDV_20220806T211755202208 06T211821_044437_054D8B_31B7	6 August 2022	VV+VH	Descending	44437
33	S1A_IW_SLC__1SDV_20220911T211756202209 0911T211823044962_055F11_FA38	11 September 2022	VV+VH	Descending	44962

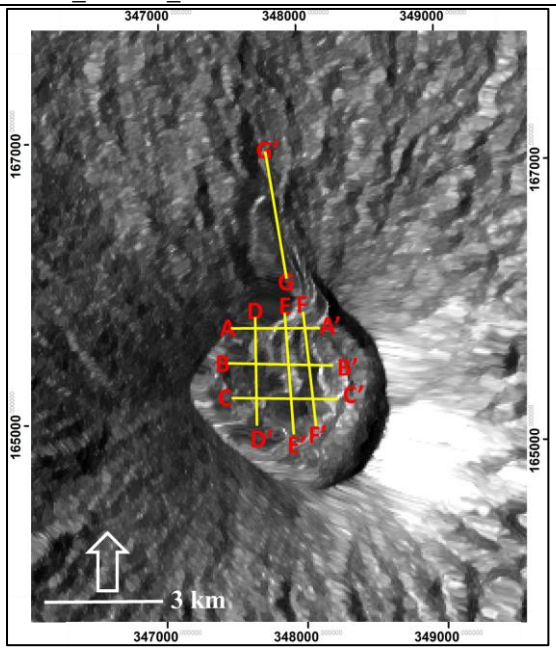

Figure 3 Sentinel-1A image on 26 May 2022 with seven cross sections (A-A', B-B', C-C', D-D', E-E', F-F', and G-G').

3 Pair-wise logic technique differential interferometric synthetic aperture radar (PLT D-InSAR) and k-means clustering

Deformation at lava dome of Mt. Ibu has been monitored using the PLT D-InSAR method. PLT D-InSAR is the development of the D-InSAR method. D-InSAR is

a phase reduction process in the deformation analysis, and atmospheric correction is necessary because the topographical components and atmospheric throttling must be removed, respectively [7]. Monitoring surface deformation using the D-InSAR method can provide spatial support for conventional vertical movement on the ground surface. The D-InSAR temporal method is an advanced synthetic aperture radar (InSAR) interferometry technique that processes several SAR images (to determine the separation of surface targets at different times as well as setting the wave delay from the atmosphere [7]. The D-InSAR method uses several pairs of interferograms at once to detect changes in surface topography with very high accuracy. D-InSAR aims to observe the movement or deformation of the ground surface using repeated-pass interferometry techniques because the changes observed are changes in the line of sight direction of the SAR sensor or line of sight (LOS). Then these changes can be measured based on wavelength units [7]. Sensor position factors and soil topography can influence the phase difference parameters as in the following equation:

$$\partial\varphi_P = -\frac{4\pi}{\lambda}\left(D_P - \frac{B\perp}{R_{1P}sin\theta_i}H_P + \in_{rr}\right) \quad (1)$$

where P is the object's surface point on the surface, λ is the wavelength used by the sensor, θ_i is the local angle of incidence, $B\perp$ is the sensor's perpendicular distance between two different times acquisition (perpendicular baseline), R_{1P} is the acquisition sensor distance at the point P, H_P are elevation heights of P above the earth's ellipsoid, and $\in_{rr}$ are wave propagation disturbances (noise) arising from atmospheric deceleration and faraday rotation [7]. Apart from D-InSAR, PLT D-InSAR was also done. In principle, the PLT D-InSAR technique attempts to overcome the waves slowing caused by the atmosphere by comparing interferograms covering different time intervals with the same data component. This method is reasonably practical for visually finding apparent deformation features caused by ionospheric disturbances [7]. Corrections made in PLT D-InSAR use simple arithmetic by sum up the two interferograms resulting from three SAR data with one SAR data used together (**Figure 3**). This approach is also called the linear combination method and is quite effective when the atmospheric anomaly is in the shared SAR data from two interferograms.

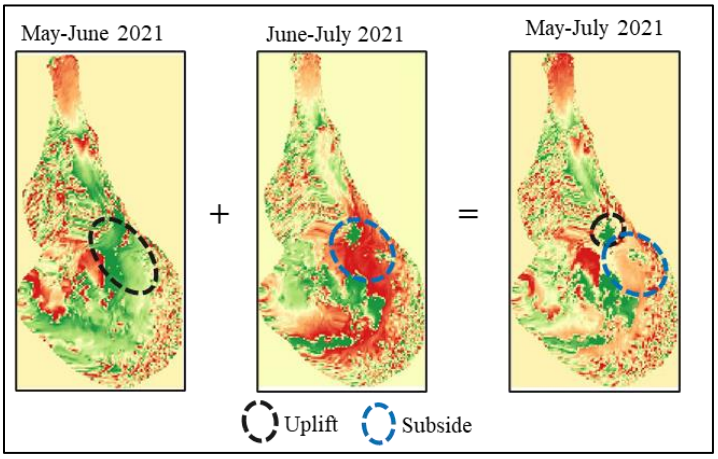

Figure 3 The sum of the two interferograms in May-June 2021 and June-July 2021 resulting an interferogram in May-July 2021. The areas in black circle (uplift) and blue circle (subside) are within one interferogram.

Apart from PLT D-InSAR, image clustering has been done based on the deformation results obtained. Deformation clustering has also been done from the previously published study by [9]. The type of clustering used is k-means clustering. The k-means clustering method is one of the clustering analysis algorithms with k being randomly selected objects as the initial clustering center [10]. The distance between each object and the initial clustering center is calculated and assigned to the nearest clustering center (centroid). This method groups the data based on the same characteristics. The k-means cluster approach is an unsupervised clustering algorithm that can group multidimensional samples into certain clusters (k) using the cost function. Suppose $C = \{C_i | \, i = 1, .., n\}$ is the K-cluster of the data set, $Z = \{z_i | \, i = 1, .., K\}$ is the center set of K [11]. This can be done by minimizing the squared error between randomly selected clusters and the samples contained in the clusters as follows [10]:

$$Cost = \sum_{i=1}^{n} dist(c_i, z_k) \quad (2)$$

where $dist(c_i, z_k)$ measures the Euclidean distance between pattern c_i and its cluster center z_k. The stages of k-means clustering are as follows [12]:

1. The centers of k initial $\{z_1, z_2, \dots, z_k\}$ must be selected randomly from n samples.
2. Sample x is assigned to cluster c if:
   $|x_i - z_j\| < \|x_i - z_p\|, p = 1,2,3, \dots, K and\ j \neq p, I = 1,2,3, \dots, n, and\ j\ \epsilon\{1,2,3, \dots, K\}$
3. Based on the equation (2), the other cluster centers $z_1 *, z_2 *, \dots, z_k *$z1$*$ should be calculated.

$$z_1 *= \frac{1}{n_i} \sum_{x_i \in C_i} x_j,\ i = 1,2,3, \dots, K$$

4. Terminate the process if centers $z_i *= z_i, I = 1,2,3, \dots, K$; if not, return to step 2.

After the clustering process, image processing has been done to the filtering stage, which aims to remove noise in the image by filtering it. In this study, we use median and open filtering. The median and opening filter removes noise in the image to get a better image contrast than the original image. In this process, noise intensity reduction is done. This process produces a smooth image and tends to eliminate noise. Then the results obtained from the deformation and k-means clustering are shown in (**Figure 4**).

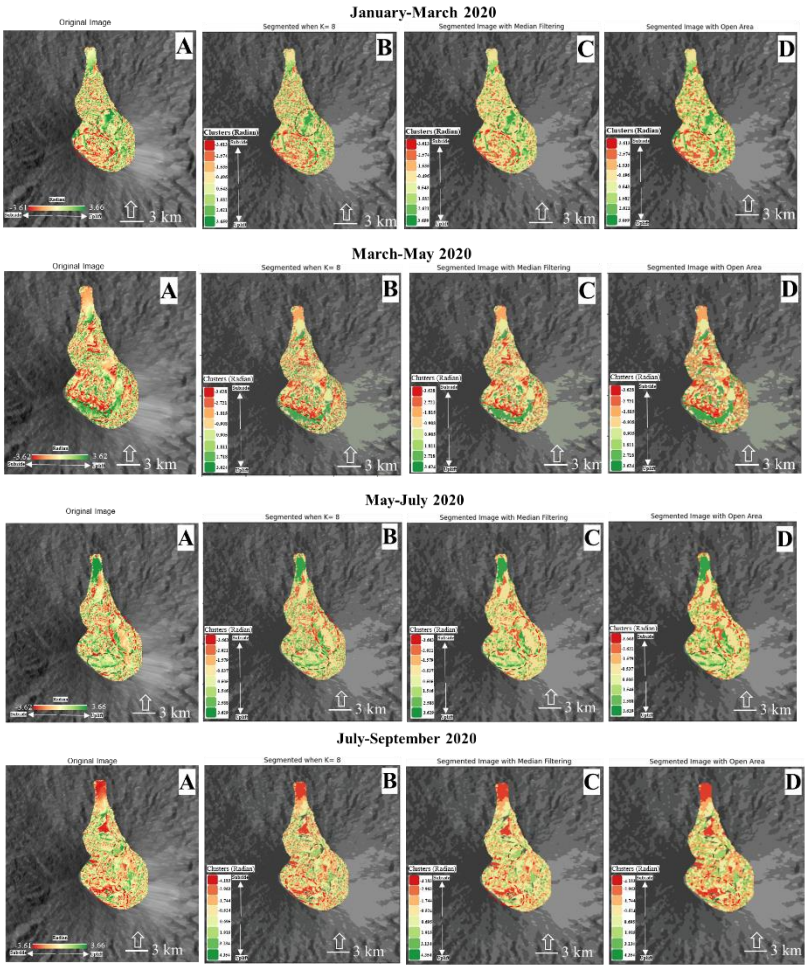

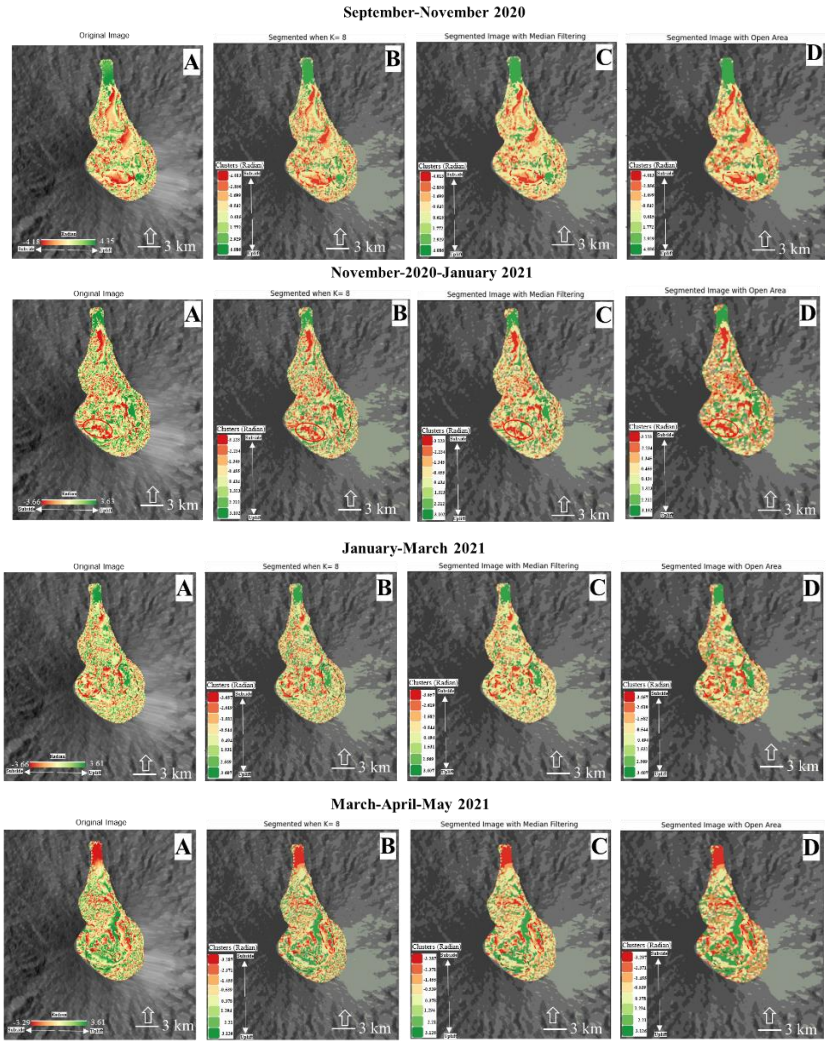
September-November 2020
Original Image
Segmented when K= 8
Segmented Image with Median Filtering
Segmented Image with Open Area
A
B
C
D
3 km
November-2020-January 2021
January-March 2021
March-April-May 2021

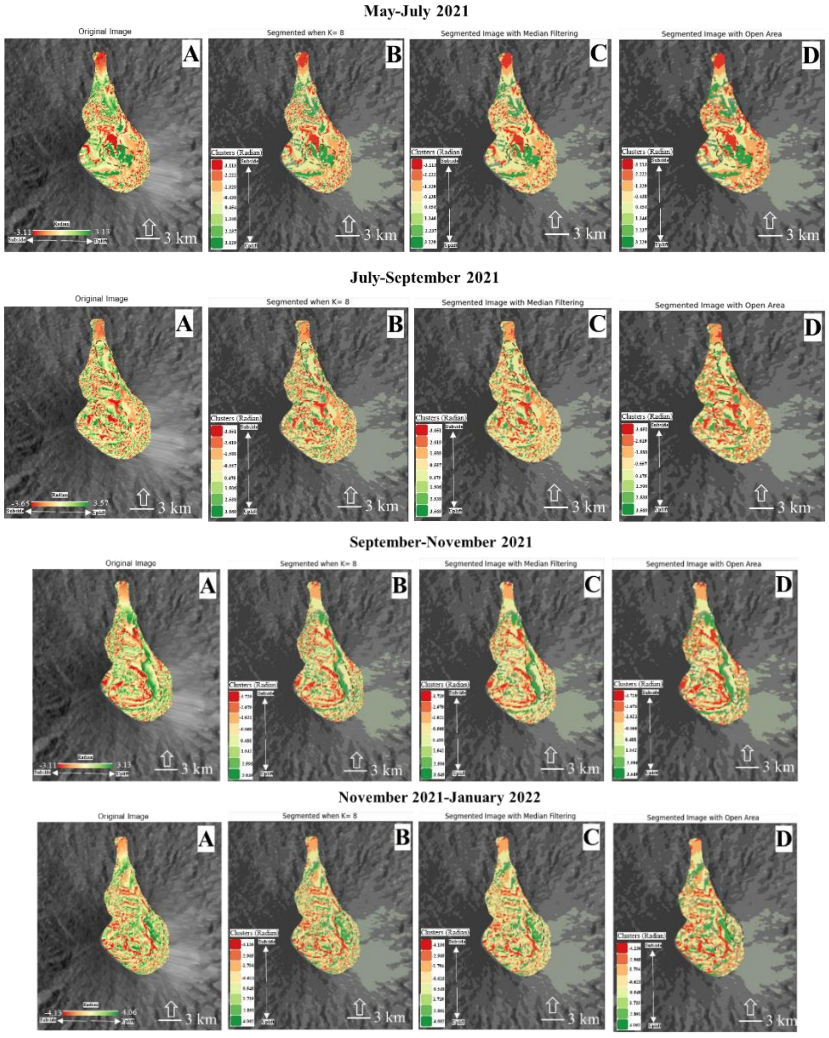
May-July 2021
Original Image
Segmented when K= 8
Segmented Image with Median Filtering
Segmented Image with Open Area
A
B
C
D
3 km
July-September 2021
Original Image
Segmented when K= 8
Segmented Image with Median Filtering
Segmented Image with Open Area
A
B
C
D
3 km
September-November 2021
Original Image
Segmented when K= 8
Segmented Image with Median Filtering
Segmented Image with Open Area
A
B
C
D
3 km
November 2021-January 2022
Original Image
Segmented when K= 8
Segmented Image with Median Filtering
Segmented Image with Open Area
A
B
C
D
3 km

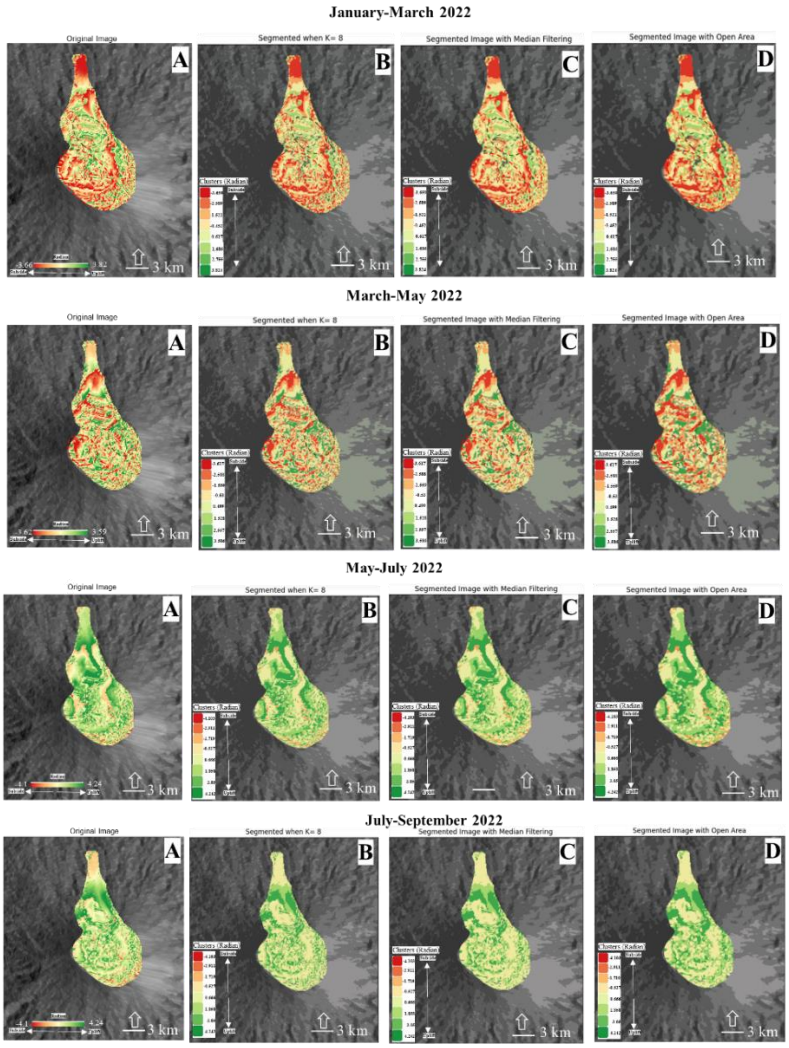

Figure 4 The interferogram generated by PLT D-InSAR method presented deformation vector of subsidence (red) and uplift (green) from January 2020 to September 2022. Original images of interferogram (A), segmented image using k-means clustering with k=8 (B), filtering image using median filtering (C), and filtering area using open filtering (D).

The PLT D-InSAR k-means clustering (k=8) image results are shown the uplift in 2020 (January, July, September, November and December), in 2021 (February, April, July and November), and in 2022 (January, March, April and August). Apart from uplift, subsidence phenomena has been occurred in 2020 (February, March, April, May, June, August and October), in 2021 (January, March, May, June, August, September, October and December), and in 2022 (February,

March, May, June, and July). Then the results of the k-means clustering (k=8) image and filtering show the noise in the segmented image is reduced, the image becomes sharpened, and values with the same characteristics as neighboring pixels are successfully grouped.

3 Discussion

Based on the results obtained from PLT D-InSAR, Mt. Ibu shows high deformation of the seven cross sections (A-A', B-B', C-C', D-D', E-E', F-F, and G-G'), which shows the highest uplift of about 0.667 m in January 2022, and the highest subsidence of about -0.48 m in August 2020 (**Figure 5**). The deformation value has been clustered using k = 6 to see its distribution on the lava dome based on time (**Figure 6**).

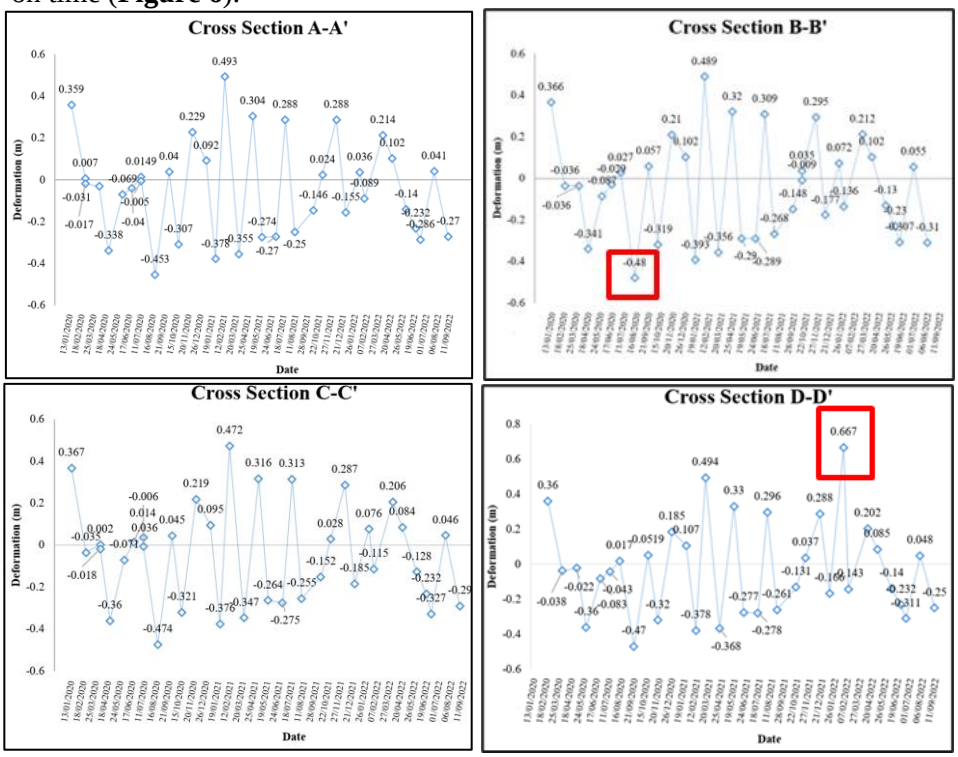

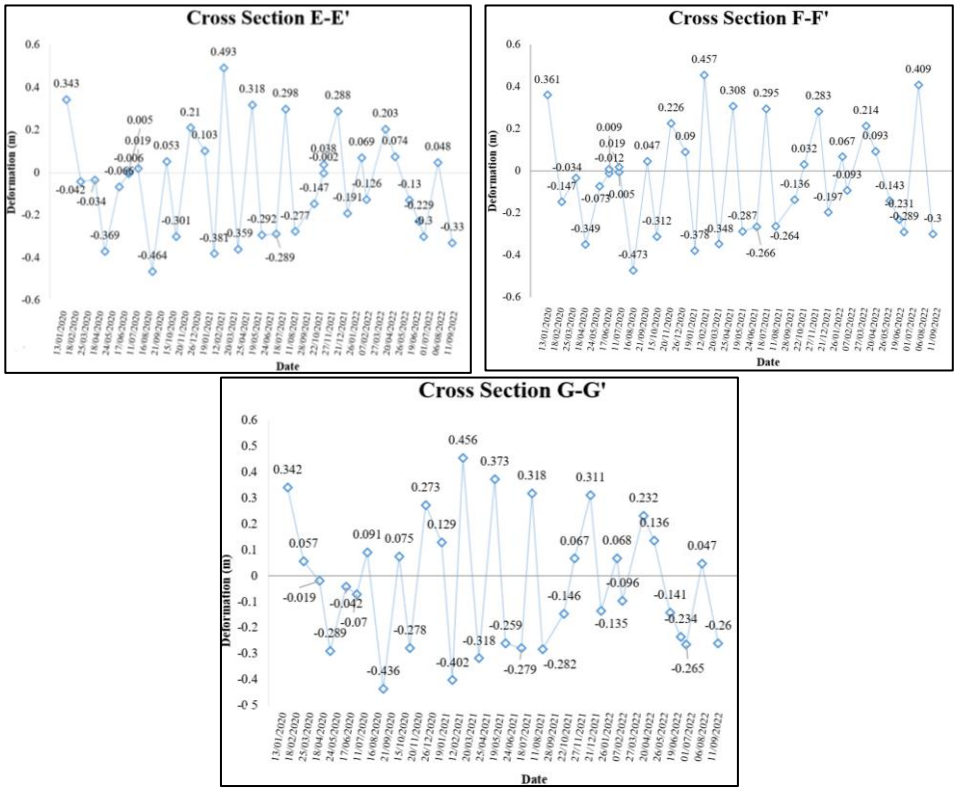

Figure 5 The deformation pattern of Mt. Ibu lava dome with subsidence deformation vector has been occurred 19 times and uplifted 14 times from January 2020 to August 2022.

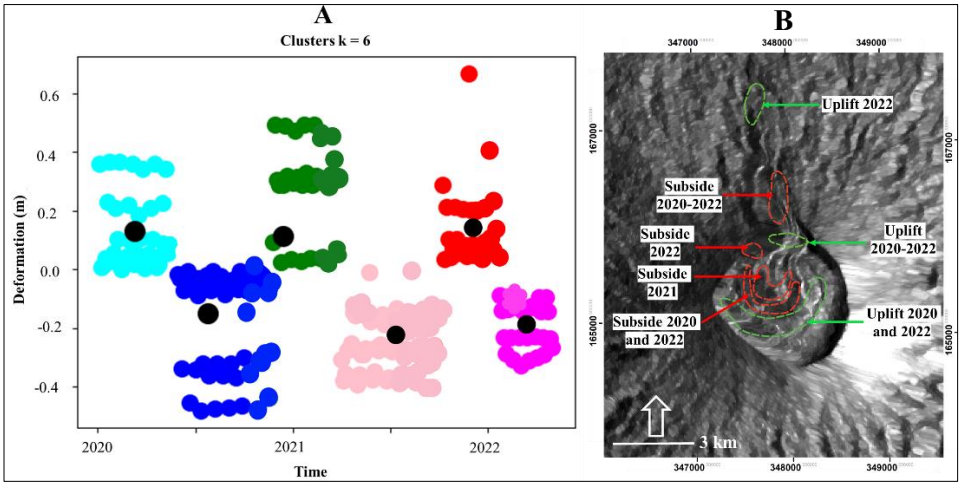

Figure 6 Clustering deformation values using cluster k=6 (A), and the distribution of deformation values based on clustering results overlaid with Sentinel-1A image (B).

Within 24 years of the first appearance of the 99-lava dome, the current Mt. Ibu is growing rapidly and has exceeded the inner crater and outer crater rim on the northern flank, thus further expanding the distribution of lava flows. Based on deformation clustering using k-means, subsidence generally occurs in the center of the lava dome, northwest, and towards the crater opening. Then the uplift generally occurs on the south of the lava dome, north on the crater opening, and north on the lava flow. Monitoring the deformation of Mt. Ibu from January 2020 to August 2022 shows that the high level of deformation is thought to have occurred due to the process of growing the lava dome which has continued to current today (September 2022). The growth of the lava dome and the direction of expansion occur due to pressure from the lava flow moving towards the crater opening, and the lava comes out through an active vent on the top of the lava dome. The deformation that occurred in the lava dome of Mt. Ibu occurs because when the growth process of the lava dome is underway, it can cause several effects such as pressure, growth cycles, lava dome decline, growth acceleration, and sudden explosive activity, as well as the disintegration of lava during the formation of pyroclastic flows, are some of the main phenomena that can occur. Causing deformation to the eruption of the lava dome [13].

4 Conclusion

In this study, the deformation at Mt. Ibu is clearly visible from PLT D-InSAR, and the k-means clustering algorithm. The results of the PLT D-InSAR deformation shows that subsidence has been occurred generally in the center of the lava dome, northwest, and towards the crater opening, and the uplift generally occurred on the south of the lava dome, north on the crater opening, and north on the lava flow. The highest uplift in January 2022 is about 0.667 m and subsidence in August 2020 about -0.48 m. Deformation analysis using PLT D-InSAR combined by k-means clustering produces clear deformation areas. This proposed method is advantage to obtain deformation at low coherence condition.

References

[1] E. S. Calder, R. Luckett, R. S. J. Sparks, and B. Voight, “Mechanisms of lava dome instability and generation of rockfalls and pyroclastic flows at Soufrière Hills Volcano, Montserrat,” *Geol. Soc. Mem.*, vol. 21, no. 1, pp. 173–190, 2002, doi: 10.1144/GSL.MEM.2002.021.01.08.

[2] C. E. Harnett and M. J. Heap, “Mechanical and topographic factors influencing lava dome growth and collapse,” *J. Volcanol. Geotherm. Res.*, vol. 420, 2021, doi: 10.1016/j.jvolgeores.2021.107398.

[3] Surono *et al.*, "The 2010 explosive eruption of Java's Merapi volcano-A '100-year' event," *J. Volcanol. Geotherm. Res.*, vol. 241–242, pp. 121–135, 2012, doi: 10.1016/j.jvolgeores.2012.06.018.

[4] USGS, "Explosions and Dome Growth, 1980-1986 and 1989-1991," 2022. https://www.usgs.gov/volcanoes/mount-st.-helens/explosions-and-dome-growth

[5] A. Saepuloh and K. Koike, "Discriminating Alteration of Pyroclastic Flow Deposits in an Active Volcano by SAR Image," in *Proceeding of the World Geothermal Congress*, 2010, no. April, pp. 25–29.

[6] A. Saepuloh, P. R. Mirelva, and K. Wikantika, "Advanced applications of Synthetic Aperture Radar (SAR) remote sensing for detecting pre- and syn-eruption signatures at Mount Sinabung, North Sumatra, Indonesia," *Indones. J. Geosci.*, vol. 6, no. 2, pp. 123–140, 2019, doi: 10.17014/ijog.6.2.123-140.

[7] A. Saepuloh, *Prinsip dan aplikasi penginderaan jauh geologi gunungapi*. Bandung: ITB Press, 2021.

[8] D. S. Vaka, S. Sharma, and Y. S. Rao, "Comparison of HH and VV Polarizations for Deformation Estimation using Persistent Scatterer Interferometry," *38th Asian Conf. Remote Sens. - Sp. Appl. Touching Hum. Lives, ACRS 2017*, vol. 2017-Octob, no. 2008, 2017.

[9] M. Cavur, J. Moraga, H. Sebnem Duzgun, H. Soydan, and G. Jin, "The DInSAR Analysis with Machine Learning for Delineating Geothermal Sites at the Brady Geothermal Field," *Proceedings*, vol. 46, no. Figure 1, pp. 1–11, 2021, [Online]. Available: https://scihub.copernicus.eu.

[10] G. Niu, Y. Ji, Z. Zhang, W. Wang, J. Chen, and P. Yu, "Clustering analysis of typical scenarios of island power supply system by using cohesive hierarchical clustering based K-Means clustering method," *Energy Reports*, vol. 7, pp. 250–256, 2021, doi: 10.1016/j.egyr.2021.08.049.

[11] R. Ghezelbash, A. Maghsoudi, and E. J. M. Carranza, "Mapping of single- and multi-element geochemical indicators based on catchment basin analysis: Application of fractal method and unsupervised clustering models," *J. Geochemical Explor.*, vol. 199, no. December 2018, pp. 90–104, 2019, doi: 10.1016/j.gexplo.2019.01.017.

[12] R. Ghezelbash, M. Daviran, A. Maghsoudi, and H. Ghaeminejad, "Applied Geochemistry Incorporating the genetic and firefly optimization algorithms into K-means clustering method for detection of porphyry and skarn Cu-related geochemical footprints in Baft district , Kerman , Iran," *Appl. Geochemistry*, vol. 148, no. November 2022, p. 105538, 2023, doi: 10.1016/j.apgeochem.2022.105538.

[13] R. S. J. Sparks, "Causes and consequences of pressurisation in lava dome eruptions," *Earth Planet. Sci. Lett.*, vol. 150, no. 3–4, pp. 177–189, 1997, doi: 10.1016/s0012-821x(97)00109-x.